

# MRI channel flows in vertically-stratified models of accretion disks

Henrik N. Latter<sup>1\*</sup>, Sebastien Fromang<sup>2,3†</sup>, Oliver Gressel<sup>4‡</sup>

<sup>1</sup> LERMA-LRA, École Normale Supérieure, 24 rue Lhomond, 75231 Paris Cedex 05, France

<sup>2</sup> CEA, Irfu, SAp, Centre de Saclay, 91191 Gif-sur-Yvette, France

<sup>3</sup> UMR AIM, CEA-CNRS-Univ. Paris VII, Centre de Saclay, 91191 Gif-sur-Yvette, France

<sup>4</sup> Astronomy Unit, School of Mathematical Sciences, Queen Mary, University of London, Mile End Road, London, E1 4NS, UK

29 October 2018

## ABSTRACT

Simulations of the magnetorotational instability (MRI) in ‘unstratified’ shearing boxes exhibit powerful coherent flows, whereby the fluid vertically splits into countermoving planar jets or ‘channels’. Channel flows correspond to certain axisymmetric linear MRI modes, and their preponderance follows from the remarkable fact that they are approximate nonlinear solutions of the MHD equations in the limit of weak magnetic fields. We show in this paper, analytically and with one-dimensional numerical simulations, that this property is also shared by certain axisymmetric MRI modes in *vertically-stratified* shearing boxes. These channel flows rapidly capture significant amounts of magnetic and kinetic energy, and thus are vulnerable to secondary shear instabilities. We examine these parasites in the vertically stratified context, and estimate the maximum amplitudes that channels attain before they are destroyed. These estimates suggest that a dominant channel flow will usually drive the disk’s magnetic field to thermal strengths. The prominence of these flows and their destruction place enormous demands on simulations, but channels in their initial stages also offer a useful check on numerical codes. These benchmarks are especially valuable given the increasing interest in the saturation of the stratified MRI. Lastly we speculate on the potential connection between ‘run-away’ channel flows and outburst behaviour in protostellar and dwarf nova disks.

**Key words:** accretion, accretion disks — MHD — instabilities — turbulence

## 1 INTRODUCTION

Differential rotation and weak magnetic fields conspire to destabilise laminar flow in accretion disks (and other astrophysical settings) via the magnetorotational instability (MRI) (Balbus and Hawley 1991). The MHD turbulence that this linear instability sustains can transport significant angular momentum, and thus drive the mass accretion that is observed in many disk systems (Hawley et al. 1995, Stone et al. 1996, Balbus and Hawley 1998, Hawley 2000).

The characteristics of MRI turbulence have been studied extensively with local three-dimensional simulations in the ‘unstratified’ shearing box<sup>1</sup>, which is a model that mim-

ics a small block of gas deeply embedded in the disk, ignorant of its large-scale vertical and radial structure (Balbus and Hawley 1998). When a net vertical magnetic flux passes through such a box, the fluid can be dominated by coherent structures (often recurring) called channel flows. Akin to Kolmogorov shear flow, these consist of several countermoving planar streams of fluid situated at different vertical levels (Meshalkin and Sinai 1961, Hawley et al. 1995, Sano and Inutsuka 2001, Sano 2007, Goodman and Xu 1994, hereafter GX94). Previous work has investigated the role these structures, and their destruction, play in controlling MRI saturation in the shearing box model (GX94, Latter et al. 2009, hereafter LLB09, Pessah and Goodman 2009, Pessah 2009). In this paper we generalise these analyses to the case of a shearing box in which the *vertical structure* of the disk has been incorporated.

however, ‘stratified’ explicitly means that the background entropy does vary.

\* Email: henrik.latter@ira.ens.fr

† Email: sebastien.fromang@cea.fr

‡ Email: o.gressel@qmul.ac.uk

<sup>1</sup> Throughout the paper we adhere to the common (mis-) use of the term ‘stratified’, by which we mean a background variation in density and pressure but not necessarily in entropy. Normally,

The preponderance of channel behaviour in unstratified boxes is connected to the fact that the channels correspond not only to linear MRI modes but also to approximate nonlinear solutions of the MHD equations, when in the incompressible, weak field limit (GX94). In this paper, we show explicitly that analogous linear modes in a vertically-stratified box possess the exact same property — they are also approximate nonlinear solutions<sup>2</sup>. This property has important consequences. It means that channel flows also dominate stratified simulations with a net vertical flux, growing exponentially and free of nonlinear interactions for a time sufficient to accumulate significant amounts of kinetic and magnetic energy. But the ultimate destruction of such a large amplitude channel can be so violent that the computational domain is evacuated of mass, and the simulation compromised (Stone et al. 1996, Miller and Stone 2000). In contrast, behaviour elicited by other magnetic configurations (a purely azimuthal field, for example) is not nearly so striking, nor numerically problematic (Miller and Stone 2000). As a result, published simulations with a net vertical field are comparatively rare, even if the magnetic configuration itself is of astrophysical importance.

The agents responsible for the disruption of isolated channel flows are nonaxisymmetric parasitic instabilities, which feed on their velocity and magnetic shear (GX94, LLB09, Pessah and Goodman 2009, Pessah 2009). In general, these parasitic modes are ineffectual until large channel amplitudes are attained because of the combined action of the background shear and the exponential growth of the channel itself. In this paper, we compute directly some of the ideal MHD parasitic modes that might be present in stratified boxes in a convenient intermediate limit. Using these results, we estimate the minimum channel amplitude that permits a successful parasitic attack. In a later article a general survey with three-dimensional simulations will be presented.

The paper is organised as follows. First, in Section 2 we present linear MRI channel modes in a vertically-stratified box and show that they are also nonlinear solutions in the limit of weak magnetic fields. These are directly computed numerically and then checked with one-dimensional stratified simulations in Section 3. Following that, in Section 4, the ideal MHD parasitic instabilities which could disrupt these channels are characterised and discussed. Our conclusions are drawn in Section 5, where we also briefly discuss the potential role of these solutions in real accretion disks.

## 2 MRI CHANNEL MODES AS NONLINEAR SOLUTIONS

We study the MRI in a ‘quasi-global’ setting, in which the vertical structure of the disk is included but the radial structure is neglected (except, of course, for the Keplerian shear). In the presence of weak magnetic fields, the essence of the

<sup>2</sup> Alternatively one could state that the Goodman and Xu channels are exact nonlinear solutions of the equations of incompressible MHD, and the solutions we present in this paper are exact nonlinear solutions of the equations of *anelastic* MHD. But, since both classes of solution leave each regime so rapidly, we prefer to call them approximate solutions to the full equations.

MRI is local, and as such is relatively impervious to the boundary conditions and larger-scale properties of the disk. Indeed, the nature of the turbulence induced by the MRI has been studied profitably in the local setting of the shearing box for over a decade. However, the inclusion of vertical structure can help us address important questions such as the relationship between the MRI, on the one hand, and on the other: magnetic buoyancy, depth-dependent ionisation, realistic radiation effects, and the formation of a disk-corona and large-scale magnetic fields (see for example, Brandenburg et al. 1995, Stone et al. 1996, Johansen and Levin 2008, Davis et al. 2010, Shi et al. 2010, Sano and Miyama 1999, Stone and Fleming 2002, Miller and Stone 2000, Hirose et al. 2006, Blackman and Pessah 2009).

The first linear axisymmetric stability analysis of the ideal MRI in a vertically-stratified local model was undertaken by Gammie and Balbus (1994) (see also the full global treatment of Papaloizou and Szuszkiewicz 1992). They addressed different equilibrium magnetic field configurations in addition to various vertical boundary conditions. Generally, the MRI eigenmodes must be calculated numerically, though some analytic progress can be made when the field is purely vertical and if it is assumed that the gas extends over all  $z$  (the ‘infinite disk’ model). These results were generalised in a more realistic geometry by Ogilvie (1998). A number of papers since have numerically computed the linear eigenmodes, usually in the context of the non-ideal MHD prevalent in protostellar disks (see, for example, Sano and Miyama 1999, Salmeron and Wardle 2003, 2005, 2008). More recently, Liverts and Mond (2009) returned to the isothermal ideal MHD infinite disk and derived analytic approximations to the linear modes with matched asymptotics in the limit of large plasma beta.

In this paper we confine ourselves to the simple case of ideal MHD and an infinite disk threaded with a vertical magnetic field. Though the axisymmetric linear MRI modes in this setting have been well-established, what has perhaps not been fully appreciated is that for large midplane  $\beta$  a subset of these linear modes (the channel flows) are approximate nonlinear solutions as well, a fact independent of the particulars of the vertical stratification. This property of stratified MRI channel flows has been suggested by some simulations (Miller and Stone 2000) and by ‘hybrid’ MRI-wind solutions (Ogilvie and Livio 2000, Salmeron et al. 2007). Here we demonstrate the result explicitly.

### 2.1 Governing equations

We study a disk of perfectly conducting fluid orbiting a massive central point with a frequency  $\Omega(r)$  (where  $r$  is cylindrical radius). Consequently, we employ the equations of ideal MHD and frame these in the geometry of the stratified shearing sheet (Goldreich and Lynden-Bell 1965, Gammie and Balbus 1994). This is the standard local approximation that describes a ‘block of disk’ centred on the midplane and at a radius  $r_0$ , and moving along the circular orbit that radius prescribes. The Cartesian coordinates  $x$  and  $y$  of the block correspond to the radial and azimuthal directions respectively. The differential rotation is accounted for by the Coriolis force and a background linear shear,  $\mathbf{u} = -2A_0x\mathbf{e}_y$ ,

where

$$A_0 = -\frac{r_0}{2} \left( \frac{d\Omega}{dr} \right)_0.$$

A Keplerian disk yields  $A_0 = 3/4$  and throughout this paper a Keplerian rotation law will always be assumed. In addition, to account for the vertical gravity of the central object, we include the force  $-\Omega_0^2 z \mathbf{e}_z$  in the momentum equation (with  $\Omega_0 = \Omega(r_0)$ ), which is simply the first term in an expansion of the gravitational potential in  $z$ . The approximation breaks down for large  $z$ , therefore we have assumed that the disk is relatively thin. From now the subscript ‘0’ will be dropped.

The governing equations of the problem are

$$\partial_t \rho = -\nabla \cdot (\rho \mathbf{u}), \quad (1)$$

$$\partial_t \mathbf{u} + \mathbf{u} \cdot \nabla \mathbf{u} = -\nabla \Phi - 2\Omega \mathbf{e}_z \times \mathbf{u} - \frac{1}{\rho} \nabla \left( P + \frac{B^2}{8\pi} \right) + \frac{\mathbf{B} \cdot \nabla \mathbf{B}}{4\pi \rho}, \quad (2)$$

$$\partial_t \mathbf{B} = \nabla \times (\mathbf{u} \times \mathbf{B}), \quad (3)$$

where the tidal potential is defined through

$$\Phi = -\frac{3}{2}\Omega^2 x^2 + \frac{1}{2}\Omega^2 z^2. \quad (4)$$

To this set we must add the equation of state and possibly the internal energy equation. We must also ensure that the magnetic field  $\mathbf{B}$  is solenoidal.

## 2.2 Equilibrium and solution ansatz

Let us suppose the disk is pierced by a weak vertical magnetic field. At some large height the magnetic field lines will most likely arc back and reenter the disk at a different radius, or perhaps plunge into the central object itself, but we neglect this larger structure, and consequently ignore any local force that a magnetic field line may exert due to the influence of its remote ‘footpoint’. We also ignore the possibility that the field lines are embedded in a hot magnetic halo. (Both cases are treated in Gammie and Balbus 1994.) The governing equations then admit the following equilibrium state:

$$\begin{aligned} \mathbf{u}_0 &= -(3/2)\Omega x \mathbf{e}_y, & \rho_0 &= \rho_{00} h \left( \frac{z}{H} \right), \\ P_0 &= P_0 \left( \frac{z}{H} \right), & \mathbf{B}_0 &= B_0 \mathbf{e}_z. \end{aligned}$$

In the above,  $h$  is a dimensionless symmetric function and  $H$  is the characteristic lengthscale of the disk’s vertical structure. The dimensional  $\rho_{00}$  and  $B_0$  are constants. In addition, there may be variations in temperature and entropy. The two functions  $h$  and  $P_0$  can be determined from the steady force and energy balances once the equation of state is specified, but their exact forms are unimportant in what follows. We require only that the stratification is convectively stable.

Consider a perturbation to the basic state, dependent on only  $z$  and  $t$ , and taking the form of a planar channel flow:

$$\mathbf{u}^{\text{ch}} = b u_0 F \left( \frac{z}{H} \right) e^{st} [\mathbf{e}_x \cos \theta + \mathbf{e}_y \sin \theta], \quad (5)$$

$$\mathbf{B}^{\text{ch}} = b B_0 G \left( \frac{z}{H} \right) e^{st} [\mathbf{e}_x \sin \theta - \mathbf{e}_y \cos \theta], \quad (6)$$

where  $F$  and  $G$  are dimensionless functions,  $s$  is a growth

rate,  $\theta$  is a constant orientation angle, and  $u_0$  and  $B_0$  constants, the latter introduced earlier in the equilibrium solution. Note also the dimensionless constant  $b$ , which measures the relative amplitude of the channel to its background at  $t = 0$ . These perturbations constitute the basic MRI.

It is easy to check that the profiles Eqs (5)-(6) possess the following attractive properties:

$$\mathbf{u}^{\text{ch}} \cdot \nabla \mathbf{u}^{\text{ch}} = \mathbf{B}^{\text{ch}} \cdot \nabla \mathbf{B}^{\text{ch}} = 0,$$

$$\mathbf{u}^{\text{ch}} \cdot \nabla \mathbf{B}^{\text{ch}} = \mathbf{B}^{\text{ch}} \cdot \nabla \mathbf{u}^{\text{ch}} = 0.$$

These cancellations mean that all the nonlinear terms in the induction equation and most of the nonlinearities in the momentum equation disappear.

Via magnetic pressure, the MRI channel flow drives perturbations in the thermodynamic variables,  $\rho^{\text{ch}}$ ,  $P^{\text{ch}}$ , etc, but these will remain small relative to the background equilibrium for as long as the magnetic field (the driving) is weak. We assume that the channel’s magnetic field is indeed weak, at least initially, and consequently *linearise* the governing equations in the thermodynamic perturbations, more specifically  $\rho^{\text{ch}}$ . The continuity equation becomes

$$\nabla \cdot (h \mathbf{u}^{\text{ch}}) = 0, \quad (7)$$

to leading order, which is satisfied by construction, and the thermodynamic perturbations drop out entirely from the  $x$  and  $y$  components of the momentum equation, i.e.  $1/\rho$  is approximated by  $1/\rho_0$  in the magnetic tension terms and we obtain

$$\partial_t \mathbf{u}^{\text{ch}} = -2\Omega \mathbf{e}_z \times \mathbf{u}^{\text{ch}} + \frac{B_0}{4\pi \rho_0(z)} \frac{\partial \mathbf{B}^{\text{ch}}}{\partial z}. \quad (8)$$

(Now all nonlinearities have vanished from these equations.) As a consequence, the  $z$  component of the momentum equation,

$$\frac{d}{dz} \left[ P^{\text{ch}} + \frac{(B^{\text{ch}})^2}{8\pi} \right] + \Omega^2 z \rho^{\text{ch}} = 0, \quad (9)$$

the equation of state, and the entropy equation are *subordinate* to the MRI dynamics. This set of ‘passive’ equations are acted upon by the MRI equations, via the channels’ magnetic pressure, but not vice-versa. Their sole job is to determine the small thermodynamic fluctuations driven by the channels and we are not obliged to solve them explicitly. Our only concern is for the magnitudes of these fluctuations, which must remain small or else the approximation breaks down. From (9) it is clear that these amplitudes, relative to their background state, are of order  $\epsilon = b^2 e^{2st} / \beta$ , where

$$\beta = \frac{2H^2 \Omega^2}{B_0^2 / (4\pi \rho_{00})}, \quad (10)$$

is the (midplane) plasma beta associated with the background vertical field. Our linearisation in  $\rho^{\text{ch}}$  is only valid for as long as  $\epsilon$  remains small.

This formalism is actually the anelastic approximation, modified so as to accommodate the MRI (Gough 1969, Gilman and Glatzmaier 1981, Barranco and Marcus 2005). Notice that the incompressible limit employed by GX94 is a special case, obtainable if we further assume the channel flows vary on scales much smaller than  $H$ .

We conclude that the channel flow ansatz introduced in Eqs (5)-(6) is not only a linear solution but also an approximate *nonlinear solution* to the governing equations in

the regime of weak magnetic field (or, equivalently, small thermodynamic fluctuations). Because the approximation introduces errors of order  $\epsilon^2$ , we expect the ansatz to fail when  $\epsilon \sim 1$ . Owing to the channels' exponential growth, this regime is achieved rapidly unless other agents intervene (such as parasitic instabilities). The time at which the approximation fails can be simply estimated by

$$t \sim \frac{1}{2s} \ln(\beta/b^2). \quad (11)$$

With a typical MRI growth rate and  $b = 0.1$  and  $\beta = 10^4$ , this time corresponds to only 1.5 orbits. But it also means that, in principle, a single MRI stratified channel can generate equipartition strength fields from very weak fields in astonishingly short times, just as its unstratified counterparts can (GX94, Hawley et al. 1995, LLB09). This is in fact witnessed in the stratified simulations of Miller and Stone (2000).

### 2.3 The eigenproblem for channel flows

We now supply the remaining details of the ansatz by deriving equations for  $F$  and  $G$  and a dispersion relation for  $s$ . The solution (5)–(6) is substituted into the governing equations so that  $\mathbf{u} = \mathbf{u}_0 + \mathbf{u}^{\text{ch}}$  and  $\mathbf{B} = \mathbf{B}_0 + \mathbf{B}^{\text{ch}}$ . After linearising in  $\rho^{\text{ch}}$ , the four equations governing the MRI channel flow are the  $x$  and  $y$  components of the momentum and induction equations. These are

$$u_0(s \cos \theta - 2\Omega \sin \theta) F = (v_A)^2 \sin \theta \left( \frac{1}{h} \frac{dG}{dz} \right), \quad (12)$$

$$u_0(s \sin \theta + \frac{1}{2}\Omega \cos \theta) F = -(v_A)^2 \cos \theta \left( \frac{1}{h} \frac{dG}{dz} \right), \quad (13)$$

$$s \sin \theta G = u_0 \cos \theta \frac{dF}{dz}, \quad (14)$$

$$(-s \cos \theta + \frac{3}{2} \sin \theta) G = u_0 \sin \theta \frac{dF}{dz}, \quad (15)$$

where  $v_A = B_0/\sqrt{4\pi\rho_{00}}$  is the equilibrium Alfvén speed at the midplane. The four functional equations can be satisfied if

$$F = -\frac{1}{Kh} \frac{dG}{dz}, \quad G = \frac{1}{K} \frac{dF}{dz}, \quad (16)$$

which together return the linear second-order ordinary differential equation:

$$\frac{d^2 F}{dz^2} + K^2 h F = 0, \quad (17)$$

where the ‘vertical wavenumber’  $K$ , a constant, is yet to be determined. Note that Equation (17) was also derived by Gammie and Balbus (1994) (cf. their Eq. (23)).

Equation (17) with suitable boundary conditions describes a 1D eigenvalue problem for the vertical MRI modes with  $K$  as eigenvalue. Because  $h$  is always positive the equation is in classical Sturm-Liouville form and so we are assured of a discrete set of real eigenvalues  $\{K_n\}$  and eigenfunctions  $\{F_n\}$ . Moreover, the eigenfunctions are orthogonal under integration with weight  $h$  (Arfken 1970). The solutions possess the symmetry  $(K_n, F_n, G_n) \rightarrow (-K_n, F_n, -G_n)$ . Notice that the lowest order solution is trivial,  $K_0 = 0$  and  $F$  a constant, but this does not correspond to the MRI.

The boundary condition comes from the requirement that the Alfvén speed of the perturbation  $(v_A^{\text{ch}})^2 \propto G^2/h$  must never diverge. Thus  $G$  (and hence  $dF/dz$ ) must go to zero at the disk boundaries. Solutions to Eq. (17) are computed in the following subsection for various equilibria.

Returning to Eqs (12)–(15), the  $z$  functions factor out and we are left with the unstratified incompressible, but discrete, dispersion relation of the MRI. Eliminating  $\theta$  and  $u_0$  we get for a given  $n$  mode

$$s^4 + (\Omega^2 + 2v_A^2 K_n^2) s^2 + v_A^2 K_n^2 (v_A^2 K_n^2 - 3\Omega^2) = 0. \quad (18)$$

If time and space are scaled by  $\Omega^{-1}$  and  $H$ , respectively, the dispersion relation only depends on the two dimensionless quantities  $\beta$  and  $n$ . Evidently, the basic physics of the MRI is shared at each separate  $z$ , and the instability is not dramatically altered by the stratification. Note that Eq. (18) was recovered in Gammie and Balbus (1994) and Liverts and Mond (2009). In the latter it appears in their Eq. (19), if one sets  $K_n = \pi(n + 1/2)/\Phi(-z_0)$  in their notation. To complete the description we need  $\theta$  and  $u_0$ , which can be computed from

$$\sin^2 \theta = -\frac{1}{6} \left( 1 - \sqrt{1 + 32 \frac{K_n^2 H^2}{\beta}} \right), \quad (19)$$

$$u_0 = \frac{3\Omega}{2K_n} \sin^2 \theta. \quad (20)$$

The quantity  $u_0/(H\Omega)$  may be regarded as the Mach number of the channel. Exactly as in the unstratified MRI, the fastest growing mode possesses the orientation angle nearest  $\pi/4$ , and the flow speed is always sub-Alfvénic (GX94, LLB09). Finally, Eq. (19) yields a critical  $\beta$  below which there can be no MRI at all: we find the critical value to be  $\beta_c = (32/15)(K_1 H)^2$ . Because the longest mode ( $n = 1$ ) will generally possess a wavenumber  $K_1 \gtrsim 1/H$ , we obtain  $\beta_c \gtrsim 2$ . This is the well-known linear result that instability is suppressed when the magnetic field (in fact, the magnetic torsional stress) is too strong (Balbus and Hawley 1991). Of course, this low  $\beta$  regime is not relevant for our large  $\beta$  nonlinear solutions.

### 2.4 Examples

#### 2.4.1 Unstratified disk

The unstratified theory (Balbus and Hawley 1991, GX94) is recovered by setting  $h = 1$  and sending the vertical boundary conditions to positive and negative infinity. Equation (17) is then the harmonic oscillator equation, and

$$F = \sin(Kz). \quad (21)$$

Because the boundary conditions have been dropped, the vertical wavenumber  $K$  is a free parameter, and because  $H$  has disappeared from the problem the plasma beta has as well. Equation (21) also corresponds to the ‘local’ (WKB) solution of (17), which assumes that the eigenfunction varies on scales much shorter than  $H$ .

#### 2.4.2 Isothermal disk

The isothermal ideal gas equation of state is  $P = c_s^2 \rho$ , where  $c_s$  is the constant sound speed. This yields a Gaussian equilibrium density stratification:  $h = \exp[-z^2/(2H^2)]$ , with

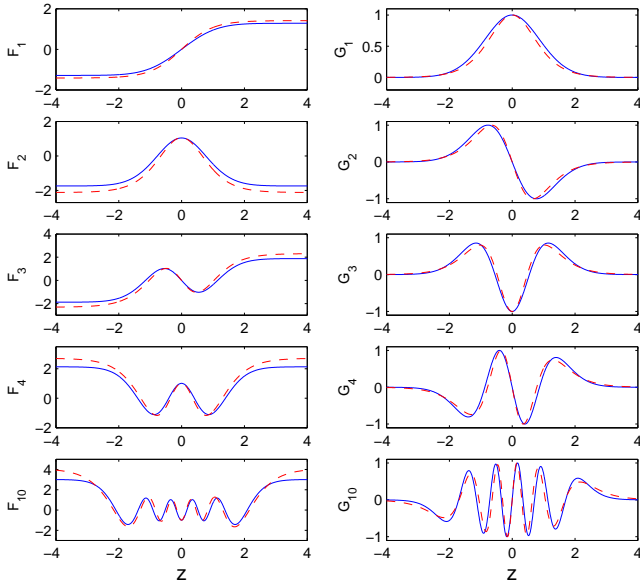


**Figure 1.** Eigenfunctions  $F_n$  and  $G_n$  of order  $n = 1, 2, 3, 4$  and  $10$  computed numerically for the isothermal model of Section 2.4.2. The functions are plotted with solid lines and are normalised so that the maximum of  $|G_n|$  is 1. The corresponding wavenumbers are  $K_n H = 1.1584, 2.0796, 2.9829, 3.8798$  and  $K_{10} H = 9.2239$ . The dashed lines are the corresponding approximations of Section 2.4.3, using the Legendre polynomials. The corresponding eigenvalues are 1.4142, 2.4495, 3.4641, 4.4641, 10.4881.

$H = c_s/\Omega$ . In this case the eigenvalue equation cannot be solved analytically. But it is a straightforward task to compute the eigenfunctions using a pseudo-spectral method. We solve for  $G$  rather than  $F$  as it decays as  $|z| \rightarrow \infty$  and so we can employ a basis of Whittaker cardinal functions (Boyd 2001, also see Section 4.4)<sup>1</sup>. MRI channel eigenfunctions are plotted in Fig. 1 for  $n = 1$  to 4 and  $n = 10$ .

As is clear, the MRI flow resemble a vertical sequence of planar ‘channels’ or ‘jets’. The centre of each jet corresponds to a magnetic null surface. This is a general result which follows from the second equation in (16): a maximum of  $F$  is a zero of  $G$ . The fluid velocities ( $F$ ) go to constant values as  $z \rightarrow \infty$ , while the magnetic fields ( $G$ ) go to zero, in accordance with the boundary conditions. When  $n$  is an even integer there exist  $n - 1$  jets, one centred at  $z = 0$ , and symmetric pairs on each side at  $\pm z_i$  for  $i = 1, \dots, (n - 2)/2$ . The  $z_i$  are the zeros of the function  $G_n$ . When  $n$  is odd there are  $n - 1$  jets occurring in antisymmetric pairs, and these are superimposed on a large-scale shear flow. In Fig. 1 this pattern can be observed; the somewhat special  $n = 1$  case corresponds to a simple shear flow (no jets), the  $n = 2$  case corresponds to a single jet centred at the midplane, the  $n = 3$  case corresponds to a double jet superimposed on a shear flow, the  $n = 4$  case to a triple jet, and so on. Finally, note that because  $K_1 = 1.158$ , we have  $\beta_c = 2.86$ .

<sup>1</sup> The numerical script that solves the isothermal eigenproblem is available on email request

### 2.4.3 Approximate isothermal model

A rough approximation to the isothermal stratification is the profile  $h = \text{sech}^2(z/H)$  (which also describes a purely self-gravitating layer — Gammie and Balbus 1994). The advantage of this choice is that it furnishes us with an analytic solution to Eq. (17). After some straightforward analysis one obtains

$$F_n = P_n[\tanh(z/H)], \quad K_n = \frac{1}{H} \sqrt{n^2 + n}, \quad (22)$$

where  $P_n$  is a Legendre polynomial of order  $n$  (Arfken 1970). These approximations are plotted in Fig. 1 as dashed lines alongside the numerical isothermal eigenfunctions. As is clear, the Legendre polynomials do an adequate job at replicating the isothermal channels, with the most noticeable discrepancies at large  $|z|$ .

### 2.4.4 Polytropic disk

A polytropic disk can be described by  $P = C \rho^{1+1/m}$  where  $m$  is the polytropic index and  $C$  is a dimensional constant. Such a disk will settle into an equilibrium density stratification of the form  $h = (1 - z^2/H^2)^m$ , where  $H$  is a combination of  $m$ ,  $C$ ,  $\Omega$ , and  $\rho_0$ , and denotes the actual disk surface — there exists only vacuum where  $|z| > H$ . For general  $m$ , the boundary value problem (17) must be solved numerically, though an analytical solution in terms of parabolic cylinder functions is available for the special case of  $m = 1$ . In Fig. 2 numerically computed solutions are presented when  $m = 3/2$ , which corresponds to an ideal gas with an adiabatic index of  $5/3$ . These are produced by a simple shooting method. We plot the first four nontrivial eigenfunctions as well as the  $n = 10$  solution. The critical plasma beta, below which there exists no unstable MRI, is  $\beta_c = 13.8$  when  $m = 3/2$ .

## 2.5 Discussion

The ‘nonlinear property’ of the channel modes permits the accumulation of significant kinetic and magnetic energies in the first few orbits of the MRI evolution. At large mid-plane  $\beta$ , small initial conditions seed a suite of fast-growing channel modes, which continue growing independently even once they reach the magnitude of the background vertical field  $\mathbf{B}_0$ . Because channels modes do not nonlinearly interact amongst themselves there may be no check on their growth until equipartition amplitudes.

There are perhaps two ways to avoid this outcome. First, parasitic modes, feeding off the MRI channels’ strong velocity shear may destroy the channel prematurely (GX94, LLB09, Pessah and Goodman 2009, Pessah 2009). We explore this in more detail in Section 4, but both unstratified and stratified simulations indicate that parasitic modes generally cannot halt the channels’ march to equipartition in the early stages of a run (Hawley et al. 1995, Miller and Stone 2000, LLB09). Second, channel flows may interact nonlinearly with slower-growing radially dependent MRI modes or, in particular, transiently growing non-axisymmetric modes (Balbus and Hawley 1992, Hawley et al. 1995). In principle, if the amplitude of the initial conditions is set equal to or above that of the background  $B_z$ , a non-axisymmetric MRI

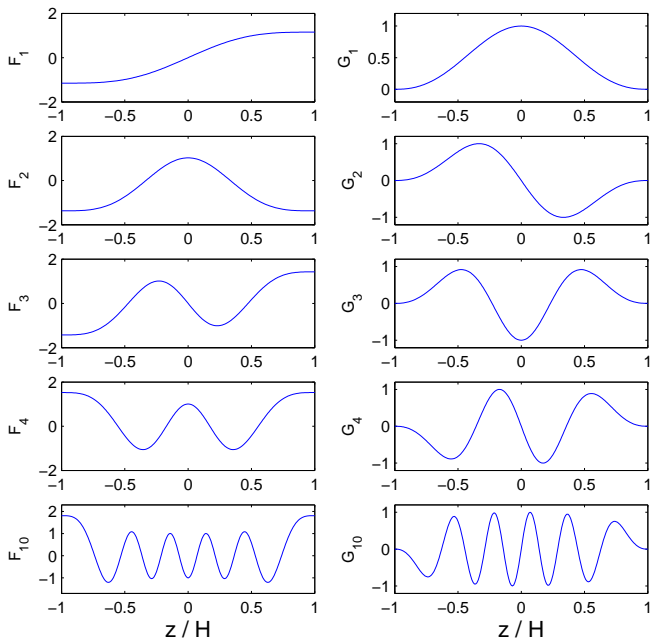


**Figure 2.** Eigenfunctions  $F_n$  and  $G_n$  of order  $n = 1, 2, 3$  and 10 computed numerically for the polytropic model of Section 2.4.4 with  $m = 3/2$ . The corresponding wavenumbers are  $K_n H = 2.541, 4.762, 6.963,$  and  $22.29$  respectively. The profiles resemble those in Fig. 1 but are confined between  $z = \pm H$ .

mode (shearing wave) could destructively interfere with a channel flow, before it dominates everything else. Indeed, seeding large-amplitude noise is a common technique in unstratified mean vertical flux simulations, as it averts the initial channel ‘spike’ (Hawley et al. 1995, LLB09). This technique should also serve in stratified simulations at intermediate and lower  $\beta$ . In very large  $\beta$  runs (as in Suzuki and Inutsuka 2009), the seeded noise is usually nonlinear from the very start.

If a channel reaches equipartition, magnetic pressure will be sufficient to alter the channel structure, squeezing mass onto the horizontal sheets where the magnetic field is zero. Some of this behaviour is explored in the following section with one-dimensional numerical simulations. The stability of these ‘extreme channel’ were studied in the unstratified context in LLB09, which showed they were undone by compressible and resistive parasitic modes.

### 3 ISOTHERMAL 1D SIMULATIONS

In this section we present a set of 1D numerical simulations using two different finite-volume 2nd order Godunov MHD codes. The purpose of these simulations is twofold. First, they will serve as a validation of the ansatz in Section 2, while conversely providing a useful numerical check on these codes. Their second aim is to determine how far into the nonlinear regime the linear channels can be followed before magnetic pressure effects become important. Obviously, an important limitation of the simulations is that they are 1D. As such, they cannot capture the parasitic modes considered

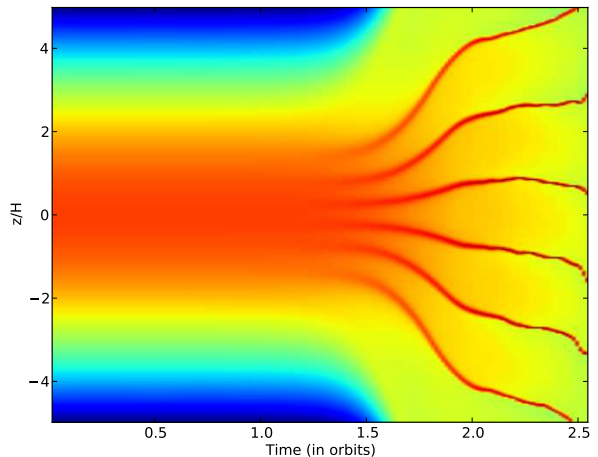


**Figure 3.** Spacetime diagram of the gas density in a simulation performed with RAMSES for  $\beta = 100$  in which a pure  $n = 7$  eigenmode is seeded at time  $t = 0$ . Density spikes develop between regions of strong magnetic field, which then lift up the thin veins of matter through magnetic buoyancy.

in Section 4, which should be studied with 3D numerical simulations.

#### 3.1 Numerical setup

We used the MHD codes RAMSES (Teyssier 2002, Fromang et al. 2006) and NIRVANA (Ziegler 2004) to solve Eqs (1)–(3) along the  $z$  direction only. An isothermal equation of state is adopted and, accordingly, the density profile at the start of the simulation is set to a Gaussian. A pure vertical magnetic field is added to this hydrostatic equilibrium, whose strength is governed by the midplane  $\beta$ . The computational domain extends in all cases from  $z = -5H$  to  $z = +5H$ , which we found was the minimum size needed for accurate results. The vertical boundary conditions are as follows: the density is extrapolated in the ghost zones in order to satisfy the vertical hydrostatic equilibrium, outflow boundary conditions are applied on the velocities, and zero-gradient boundary conditions are applied to the tangential component of the magnetic field (in 1D, the vertical field is constant in space and time). At  $t = 0$ , we either seed the isothermal eigenmodes calculated in Section 2.4.2 or their approximation in terms of Legendre polynomials, outlined in Section 2.4.3. In both cases, their amplitudes are such that the maximum value of the horizontal magnetic field is a fraction  $b$  of the vertical field  $B_0$ .

#### 3.2 The case $\beta = 10^2$

We first consider the case  $\beta = 10^2$ . Admittedly, this is a choice that does not best demonstrate the nonlinear property of the channel flows: the channels can grow only a few times  $B_0$  before hitting equipartition. However, lower  $\beta$  runs facilitate a clean comparison of the growth rates and eigenfunctions, because the various modes are fewer and relatively well-spaced.

Mode number	$\sigma_{\text{th}}/\Omega$	$\sigma_{\text{num}}/\Omega$ RAMSES	$\sigma_{\text{num}}/\Omega$ NIRVANA
$\beta = 100$			
n=1	0.2664	$0.2662 \pm 0.0001$	$0.2674 \pm 0.0009$
n=2	0.4307	$0.4302 \pm 0.0001$	$0.4276 \pm 0.0001$
n=3	0.5502	$0.5495 \pm 0.0002$	$0.5471 \pm 0.0002$
n=4	0.6363	$0.6353 \pm 0.0003$	$0.6330 \pm 0.0002$
n=5	0.6957	$0.6944 \pm 0.0003$	$0.6920 \pm 0.0002$
n=6	0.7326	$0.7307 \pm 0.0003$	$0.7290 \pm 0.0002$
n=7	0.7489	$0.7463 \pm 0.0003$	$0.7458 \pm 0.0003$
n=8	0.7455	$0.7414 \pm 0.0004$	$0.7427 \pm 0.0004$
n=9	0.7214	$0.7153 \pm 0.0004$	$0.7148 \pm 0.0005$
n=10	0.6744	$0.6653 \pm 0.0003$	$0.6618 \pm 0.0003$
$\beta = 1000$			
n=20	0.7343	$0.7308 \pm 0.0008$	$0.7174 \pm 0.0005$
n=30	0.7133	$0.6921 \pm 0.0038$	$0.6989 \pm 0.0012$
$\beta = 100$ –Legendre Approximation			
n=4	0.6363	$0.6357 \pm 0.0041$	$0.6374 \pm 0.0041$
n=7	0.7489	$0.7413 \pm 0.0033$	$0.7435 \pm 0.0012$
n=10	0.6744	$0.6677 \pm 0.0089$	$0.6737 \pm 0.0064$

**Table 1.** Growth rates of the normal modes of order  $n$  (first column) obtained with the codes RAMSES (third column) and NIRVANA (fourth column). The second column display the theoretical growth rates for the purpose of comparison. The data under the heading ‘Legendre Approximation’ were obtained with runs in which the initial condition was an approximate isothermal eigenfunction (cf. Section 2.4.3); all other runs were seeded with the correct isothermal eigenfunction (computed in Section 2.4.2).

We set  $b = 0.01$  and seed as initial conditions the isothermal eigenfunctions of Section 2.4.2 with  $n$  values between 1 and 10. For this range of parameters, we find a resolution of  $N_z = 256$  gridpoints to be mandatory in order to properly reproduce the mode morphology. This amounts to about 25 cells per scaleheight. For each  $n$ , we measure the growth rates with both RAMSES and NIRVANA. They are reported in Table 1, in the third and fourth columns respectively, while the second column gives the expected theoretical growth rate computed using Eqs (17) and (18) with the isothermal model. For all  $n$ , the agreement between the numerical results and the analytical prediction is excellent, cross-validating both results. It should be noted, though, that it is difficult to follow the  $n = 1$  mode for longer than 1.5 orbits (at which point the eigenmode has grown by only about an order of magnitude). Because  $\sigma_{\text{num}}$  is so small for this mode, any numerical error tends to seed higher order rapidly-growing eigenmodes that quickly overcome the seeded  $n = 1$  mode.

Finally, we comment briefly on the nonlinear evolution of the eigenmodes. A spacetime diagram of the density field  $\rho$  for the seeding of a  $n = 7$  mode is presented in Fig. 3. No features are apparent when  $t < 1.3$  orbits, corresponding to the weak-field, anelastic phase of the evolution. At near  $t = 1.3$  orbits the amplitude of the channel magnetic field is already a few times that of the vertical field  $B_0$ , yielding a midplane  $\beta$  of order 10. At later times, or rather smaller  $\beta$ , magnetic pressure fluctuations compress the density into

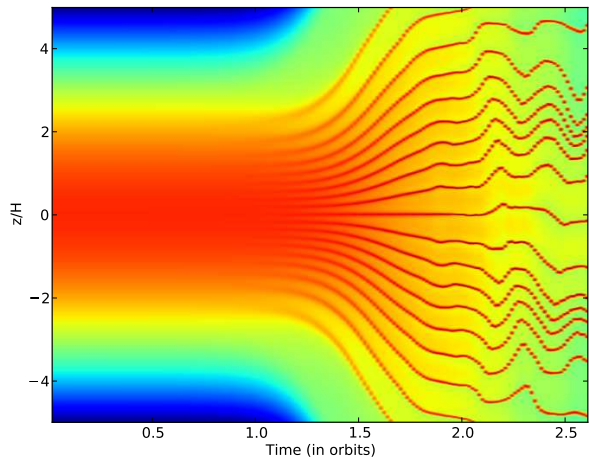


**Figure 5.** As in Fig. 3 but in the case  $n = 20$  and  $\beta = 1000$ .

thin layers that are then lifted up by magnetic buoyancy. This is similar to the results of past 3D numerical simulations of the MRI in the shearing box in the presence of a vertical flux (Miller and Stone 2000).

### 3.3 The cases $\beta = 10^3$ and $\beta = 10^4$

We also perform 1D simulations with  $\beta = 10^3$  and  $\beta = 10^4$ , both with  $b = 0.1$ . These larger  $\beta$  values offer more opportunity for the channel flows to confirm that they are indeed good approximate nonlinear solutions.

When  $\beta = 10^3$ , the fastest growing eigenmodes are those with  $n$  values between  $n = 20$  and  $n = 30$ . To adequately describe these modes, a resolution of  $N_z = 512$  is required. This corresponds to more than 50 cells per scaleheight. A lower resolution is unable to represent the high spatial frequencies of the profiles. Despite these large spatial resolution, we are unable to follow the growth of low order modes. This is again because their growth rates are so comparatively small: numerical errors seed higher order modes that grow faster and quickly distort their low order precursors.

We present the results of two simulations, the first initialised with a  $n = 20$  mode and the second with a  $n = 30$  mode. The growth rates of both are reported in Table 1. Similarly to the  $\beta = 100$  runs, there is excellent agreement between the analytical and the numerical  $\sigma$ ; moreover the linear modes hold their spatial profiles up to large amplitudes. The latter point is illustrated in the left panel of Fig. 4, in which the vertical profile of  $B_x/B_0$  is shown (solid line) at time  $t = 1.1$  orbit. The dashed line shows the same function at time  $t = 0$ , appropriately rescaled in order to match the amplitude of the eigenmode at  $t = 1.1$ . The two profiles are in good agreement, even though the mode has grown by about two orders of magnitude, and at  $t = 1.1$  is nearly one order of magnitude greater than the background field  $B_0$ . After  $t = 1.1$ , the midplane  $\beta$  dips below 10, and the subsequent evolution mirrors that of the  $\beta = 100$  runs. This nonlinear behavior is illustrated in Fig. 5, a spacetime diagram for the density in the case  $n = 20$ .

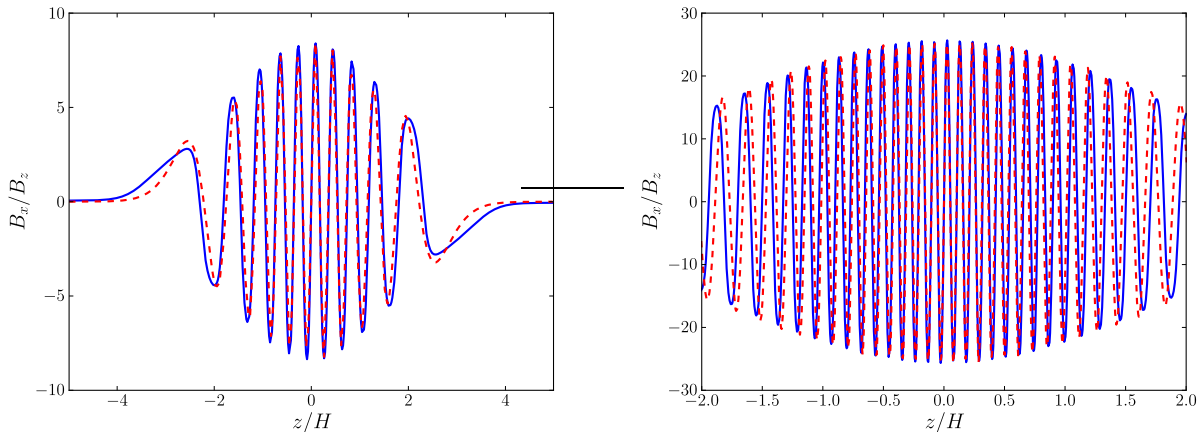


**Figure 4.** Left panel: Vertical profile of  $B_x/B_0$  (*solid line*) at time  $t = 1.1$  orbits for a simulation performed with RAMSES in which an exact normal mode of order  $n = 20$  is seeded initially with  $\beta = 10^3$ . The dashed line shows the vertical profile of  $B_x$  at  $t = 0$ , rescaled in order to match the amplitude of the field at  $t = 1.1$ . Right panel: as in the first panel, but with  $\beta = 10^4$ , a seeded  $n = 68$  mode, and after  $t = 1.3$ . The domain has been truncated to better display the fine-scale structure.

When  $\beta = 10^4$ , the fastest growing eigenmode is  $n = 68$ . Due to its fine-scale structure, a resolution of  $N_z = 2048$  is required to describe it. This corresponds to more than 200 cells per scaleheight (which in 3D would amount to a formidable computational challenge). As in the previous examples, the numerical growth rate compares well with the analytic prediction: the former is  $0.7398 \pm 0.00018$  (with RAMSES), while the latter is 0.7424. In the right panel of Fig. 4 the channel’s vertical profile of  $B_x/B_0$  is plotted when  $t = 0$  (*dashed line*) and when  $t = 1.3$  (*solid line*), with the  $t = 0$  profile rescaled. Because the rapid spatial oscillations are difficult to see, we truncate the figures at  $\pm 2H$ . Note that by  $t = 1.3$  the channel has grown by some 25 times the background vertical field, but the agreement between the two profiles remains excellent. Discrepancies emerge first at intermediate  $z$ . This is because the (depth-dependent) plasma beta associated with a channel is somewhat smaller at a few scale heights and compressible physics distort the original profile in these layers before the others. Thus equipartition will first emerge not at the midplane but at a few scale heights. But this effect is only noticeable at larger  $n$ .

### 3.4 Legendre polynomial approximation

We also test the soundness of the approximation introduced in Section 2.4.3. To do that, we perform simulations in which are seeded the approximate eigenmodes of Eq. (22), though still with the standard Gaussian profile for the equilibrium density. For  $\beta = 10^2$  and  $n$  between 4 and 10 we find the approximate modes hold their vertical profiles relatively well throughout the time evolution. This is illustrated in Fig. 6, which compares the vertical profile of  $B_x/B_0$  obtained with RAMSES at time  $t = 1.2$  orbits in simulations in which the exact eigenmodes are seeded (*solid line*) with the results obtained when the Legendre approximation is seeded (*dashed line*). The three panels, from left to right, respectively correspond to the case  $n = 4$ ,  $n = 7$ , and  $n = 10$ . The  $n = 7$  mode is the fastest growing and it offers excellent agreement between both solutions. The agreement is acceptable in the

other two cases, though not so striking. The discrepancy here follows simply from the smaller growth rates of these modes. The Legendre profiles, being approximations, possess small components in the ‘eigendirections’ of faster growing exact modes. Over time, these small perturbations, enjoying larger growth rates, will distort the evolution of the seeded approximation, resulting in the imperfect first and third profiles of Fig. 6. Nevertheless, these deviations are controlled and fail to modify the growth rate significantly, as shown in the third part of Table 1 for the modes  $n = 4, 7$  and 10. For values of  $n$  smaller than four and larger than ten, we found that such problems become important and the Legendre approximation breaks down. This is a problem for larger  $\beta$ , where there are more growing modes at larger  $n$ . At any given time, however, the set of Legendre polynomials offers a useful approximate spectral decomposition of any stratified flow into its component MRI modes. This point will be explored in more detail in a forthcoming numerical paper.

## 4 PARASITIC INSTABILITIES

Stratified channel flows will be subject to secondary ‘parasitic’ instabilities (GX94, LLB09, Pessah and Goodman 2009, Pessah 2009), which can feed on their strong velocity shear, and if resistivity is present, on their magnetic shear (both evident in Figs 1 and 2). This section concerns the behaviour of these secondary instabilities, characterising them mathematically in a convenient intermediate limit of channel amplitude. Their role in the destruction of MRI channels is then discussed, as well as their importance in sustained MRI-induced turbulence.

### 4.1 Intermediate asymptotic limit

The parasitic analysis is complicated by the fact that the equilibrium state that we are perturbing varies with  $x$  and  $t$  (in addition to  $z$ ). In shearing coordinates the  $x$  dependence can be removed, but the time dependence remains:

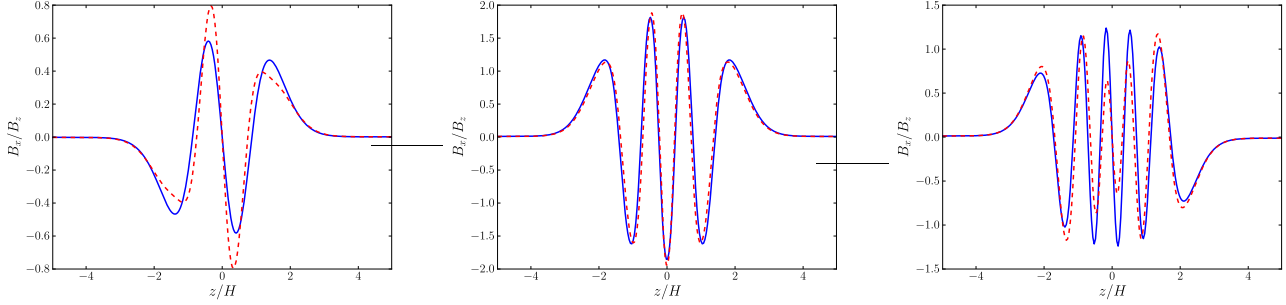


**Figure 6.** In each panel the solid line represents the vertical profile of the radial component of the magnetic field (*solid line*) after  $t = 1.2$  orbits for seeded isothermal modes of  $n = 4$  (*left panel*),  $7$  (*middle panel*) and  $10$  (*right panel*), all with  $\beta = 10^2$ . The dashed lines represent results obtained when the Legendre approximations to these modes are seeded.

the channel flow grows exponentially like  $e^{st}$ , and the background linear shear flow, issuing from Keplerian rotation, will ‘shear out’ non-axisymmetric disturbances over time.

To get around these difficulties, we assume that the parasitic modes grow on a timescale much faster than the channel growth time and the Keplerian shear time (GX94). This, in fact, corresponds to an assumption concerning the amplitude of the channels themselves, and is equivalent to  $b \gg 1$ . So the channels must take large amplitudes — much larger than the amplitude of the vertical equilibrium field  $\mathbf{B}_0$ . But if we want to use the convenient channel profiles computed in Section 2, these amplitudes cannot be too big, for if they were, then the ansatz, Eqs (5)–(9), would fail to hold. More precisely, the midplane Alfvén speed associated with the channel  $v_A^{\text{ch}}$  must be much bigger than the midplane Alfvén speed of the vertical background  $v_A$ , and concurrently much smaller than the sound speed  $c$ . This leads to the restriction

$$1 \ll b \ll \sqrt{\beta}. \quad (23)$$

Obviously, in order for this intermediate range of amplitudes to exist, the initial  $\beta$  must be sufficiently large. Once this assumption is made, we can use the vertical channel structures given by Eq. (17), while neglecting their exponential growth, the Keplerian shear, Coriolis force, and vertical background field. These simplifications transform the channel computation into a 1D eigenvalue problem in  $z$ .

## 4.2 Governing equations

We perturb the channel solution with a small incompressible disturbance, so that

$$\mathbf{u} = \mathbf{u}_0 + \mathbf{u}^{\text{ch}} + \mathbf{u}', \quad \mathbf{B} = \mathbf{B}_0 + \mathbf{B}^{\text{ch}} + \mathbf{B}', \quad \Psi = \Psi_0 + \Psi',$$

where  $\Psi$  denotes total pressure and the prime designates the parasites. For simplicity we have neglected the small variations in the total pressure introduced by the channel itself. We have also ignored buoyancy effects associated with the background vertical pressure structure, which will have a small stabilising influence on the channel’s strong velocity shear (Drazin and Reid 1982). Together with the incompressibility assumption, these approximations are particularly valid when  $K_n$  is large, which corresponds to the regime of interest. The disturbances are substituted into the gov-

erning equations and we linearise in the small parasitic disturbances. We next assume that  $b$  is large and that the time dependence of the parasites scales like  $\partial_t \sim b\Omega$ . This allows the dropping of the background Keplerian shear  $\mathbf{u}_0$ , Coriolis force, and the exponential growth of the channel to leading order. Throughout most of the domain, this also means that the background vertical field  $\mathbf{B}_0$  is also subdominant, except far from the midplane where  $\mathbf{B}^{\text{ch}}$  goes to zero. However, it can be shown that the contribution of the background vertical field in these regions makes little difference to the overall solution. Consequently, as far as the parasitic mode is concerned, the equilibrium is to leading order *stationary*, and we are permitted to take normal modes:

$$\mathbf{u}', \mathbf{B}', \Psi' \propto e^{ik_x x + ik_y y + \sigma t},$$

where  $k_x$  and  $k_y$  are (real) wavenumbers and  $\sigma$  is a growth rate. Next, we adopt space and time units so that  $H = 1$ , and  $b\Omega = 1$ , while scaling the velocity, magnetic field, and pressure by  $bu_0$ ,  $bB_0$ , and  $b^2 u_0^2 \rho_{00}$  respectively. This scaling removes the parameter  $b$  from the problem directly. Also, we solve for linear momentum density  $\mathbf{p}'$ , defined through

$$\mathbf{p}' = h(z) \mathbf{u}', \quad (24)$$

in place of the velocity. The linearised equations for  $\mathbf{p}'$ ,  $\mathbf{B}'$ , and  $\Psi'$  are now:

$$\begin{aligned} \sigma \mathbf{p}' = & -M \left[ p'_z \partial_z \hat{\mathbf{u}} + i(\mathbf{k} \cdot \hat{\mathbf{u}}) \mathbf{p}' + (i\mathbf{k} + \mathbf{e}_z \partial_z) \Psi' \right] \\ & + \frac{2}{\beta M} \left[ B'_z \partial_z \hat{\mathbf{B}} + i(\mathbf{k} \cdot \hat{\mathbf{B}}) \mathbf{B}' \right], \end{aligned} \quad (25)$$

$$\sigma \mathbf{B}' = M \left[ B'_z \partial_z \hat{\mathbf{u}} - p'_z \partial_z \hat{\mathbf{B}}/h + i\mathbf{p}'(\mathbf{k} \cdot \hat{\mathbf{B}})/h - i\mathbf{B}'(\mathbf{k} \cdot \hat{\mathbf{u}}) \right], \quad (26)$$

$$0 = i\mathbf{k} \cdot \mathbf{p}' + \partial_z p'_z - \partial_z (\ln h) p'_z, \quad (27)$$

where  $\mathbf{k} = k_x \mathbf{e}_x + k_y \mathbf{e}_y$ , the channel background is represented by the ‘hatted’ vectors:

$$\begin{aligned} \hat{\mathbf{u}} &= F_n(z) (\mathbf{e}_x \cos \theta + \mathbf{e}_y \sin \theta), \\ \hat{\mathbf{B}} &= G_n(z) (\mathbf{e}_x \sin \theta - \mathbf{e}_y \cos \theta), \end{aligned}$$

and where we have introduced the Mach number

$$M = u_0 / (H\Omega) \quad (28)$$

which can be computed from Eq. (20). Equations (25)–(27) describe a one-dimensional eigenvalue problem with eigenvalue  $\sigma$ . The boundary conditions require that all variables go to zero at the disk’s vertical boundaries.

The inputs for the eigenproblem include: the function  $h$  (representing the equilibrium density stratification), the parameter  $\beta$  (representing the strength of the vertical magnetic field), the integer  $n$  (which fully defines the channel flow), and  $k_x$  and  $k_y$  (which define the horizontal variation of the parasitic mode). In place of the last two it is convenient to use  $k = \sqrt{k_x^2 + k_y^2}$  and  $\theta_k = \arctan(k_y/k_x)$ . These are just the horizontal wavevector magnitude and its orientation with respect to the  $x$  and  $y$  axis. It is also helpful in some circumstances to use  $\Delta = \theta - \theta_k$ , which measures the difference in orientation between a parasite's wavevector and the direction of the channel flow. All the other quantities and functions that appear in the equations —  $K_n$ ,  $F_n$ ,  $G_n$ ,  $\theta$ ,  $M$  — depend solely on  $h$ ,  $\beta$ , and  $n$ , through Eqs (17), (19), and (20).

### 4.3 Asymptotic analysis

The full set of equations are solved numerically for general parameters, but some analytic expressions can be obtained in the limit of small  $k$ . These provide a check on the numerics and also offer some physical insight. The details of the analysis can be found in Appendix A; in this subsection we briefly summarise some of the results pertaining to the fastest growing parasitic mode.

As in GX94 and LLB09, the parasites can be classed into two main types. There is the Type 1, Kelvin-Helmholtz or kink, mode which attacks every jet in the sequence of MRI channels, vertically buckling each in the familiar sinusoidal pattern. Then there are the Type 2, or kink-pinch, modes, which kink some of the jets, but attack others via an alternate vertical squeezing and stretching, in a pattern something akin to a sausage (see LLB09). The latter ‘hybrid’ modes always grow slower than the kink mode, usually by an order of magnitude. Because such modes will rarely destabilise a channel, and their asymptotic analysis is quite involved, we do not discuss them in this subsection.

In the limit of very long horizontal wavenumber  $0 < k \ll 1$ , the leading order features of the kink mode are relatively easy to ascertain. Its growth rate is given by

$$\sigma^2 = A_n k^2 M^2 [\cos^2 \Delta - M_A^{-2} \sin^2 \Delta], \quad (29)$$

where  $A_n$  is a positive number dependent on the channel profile (see Appendix A), and the Alfvénic Mach number is  $M_A = u_0/v_A^0 = M\sqrt{\beta}/2$ . The latter depends on  $\theta$ , but it will always be less than 1. The growth rate scales like  $k$ , and the modes will stabilise when

$$|\theta - \theta_k| > \arctan M_A. \quad (30)$$

The stability criterion above is exactly that of parasitic kink modes in the unstratified case (GX94, LLB09). The kink mode favours orientations of its wavevector near the direction of the channel flow; the more  $\mathbf{k}$  points away from  $\mathbf{u}^{\text{ch}}$ , the less shear energy is available and the greater the stabilising magnetic tension. When the angle difference  $|\theta - \theta_k|$  is larger than some number less than  $\pi/4$  the mode stabilises. Conversely, the fastest growing modes are oriented parallel to the channel,  $\theta = \theta_k$ , and being perpendicular to the magnetic field, are essentially hydrodynamic.

### 4.4 Numerical solutions

The Eqs (25)–(27) are solved numerically via a pseudospectral method similar to that employed in LLB09 but using Whittaker cardinal functions (as in Section 2.4.2) rather than Fourier modes. The Whittaker basis is convenient because it ensures all solutions obey the decaying boundary conditions far from the midplane (Boyd 2001). If  $N$  functions and a (uniform) grid spacing of  $\delta z$  are employed, the governing equations reduce to a generalised algebraic eigenvalue problem of order  $7(N/\delta z)$ , the spectrum (or some portion of the spectrum) of which may be obtained by the QZ algorithm, or an Arnoldi method (Golub and van Loan 1996). Setting  $N = 16$  and  $\delta z = 0.04$  sufficed in most cases, though these must be improved upon if one is to resolve solutions when  $n$  is large (because of the channels’ and their parasites’ finer spatial structure). In order to simplify the problem we assume that the disk and the MRI modes can be represented adequately by the approximate isothermal model of Section 2.4.3.

As in LLB09, the eigenproblem is subject to many parameters and exhibits a rich variety of mode behaviour. In particular, when  $n$  increases the number and complexity of the set of unstable modes is striking. However, we may always decompose this suite of instabilities into (a) a single ‘pure’ kink mode, and (b) a subset of slower growing (and more physically complicated) kink-pinch modes. To ease their presentation, we restrict ourselves to hydrodynamical modes only; that is, we set  $\theta = \theta_k$ . In practice these turn out to be the fastest growing, and therefore the most dynamically significant. For the same reason, we concentrate our attention primarily on the kink mode, and do not catalogue the physical intricacies of the many kink-pinch modes that emerge: they just grow too slowly. Finally, we specialise to the case  $\beta = 1000$ . This value permits only a marginal satisfaction of Eq. (23), but facilitates the calculation. In any case, the general structure of the solutions are relatively impervious to  $\beta$ . This leaves the two parameters  $n$  and  $k$ . When  $\beta = 1000$  there exist growing channel flows for all  $n \leq 38$ , with the fastest growing channel possessing  $n = 21$ . We present detailed results for only two cases  $n = 2$  and  $n = 10$ , as these summarise neatly the overall behaviour. In both cases,  $k$  is allowed to vary smoothly from 0 to near  $K$ , at which point the parasitic modes stabilise. The results for the  $n = 21$  mode are complicated, but are similar overall to the  $n = 10$  case.

#### 4.4.1 The $n = 2$ MRI channel flow: a single jet

The somewhat special  $n = 1$  channel flow is a simple shear layer (see Fig. 1), and, as expected, yields only one parasitic mode. This is the classical Kelvin-Helmholtz instability, which achieves its fastest growth when  $k \approx K/2$  and is extinguished when  $k \gtrsim K$  (for  $n = 1$ ,  $K = 1.1584$ ). The  $n = 2$  channel flow consists of a single jet centred on the midplane, and is in fact a close relative of the  $\text{sech}^2 z$  ‘Bickley jet’ (Bickley 1937). Consequently, it is subject to two parasitic instabilities, the classical kink and pinch (see Drazin and Reid 1981, Biskamp et al. 1998, LLB09). The growth rates of each as a function of  $k$  are plotted in Fig. 7. As is typical, the growth rate of the kink mode is significantly larger than the pinch mode, and extends over a wider range

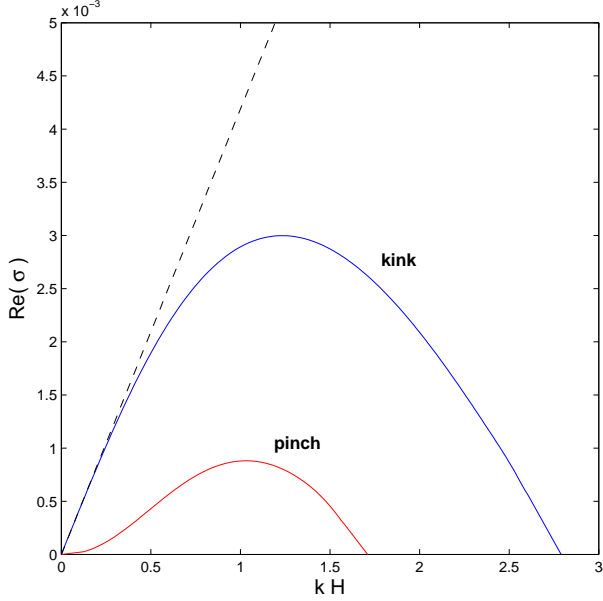


**Figure 7.** Growth rates of the unstable kink and pinch mode attacking the  $n = 2$  MRI channel, which is a single magnetised jet centred at  $z = 0$ . The plasma beta  $\beta$  is set to 1000. The growth rates are plotted as functions of  $kH$ , while  $\theta_k = \theta$ . The latter restriction means the modes are essentially hydrodynamic. The asymptotic estimate of  $\sigma$  for the kink mode, cf. Eq. (29), is plotted with a dashed line.

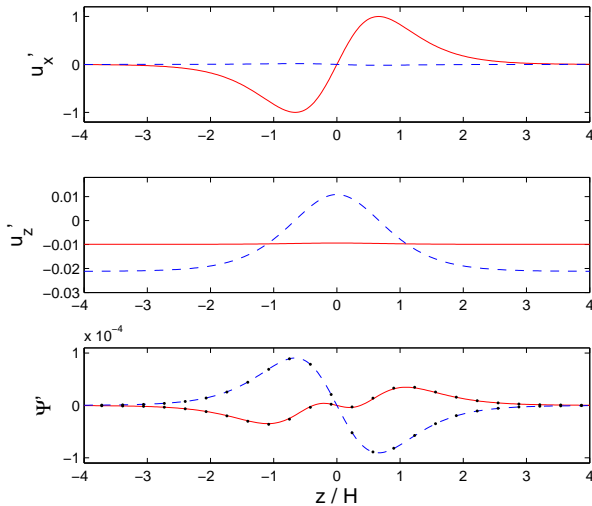


**Figure 8.** The  $u'_x$ ,  $u'_z$  and  $\Psi'$  eigenfunctions of a kink mode attacking the  $n = 2$  channel. Here  $k = 0.01K (= 0.0245)$ ,  $\theta_k = \theta$ , and  $\beta = 1000$ . The solid lines indicate real part and dashed lines indicate imaginary part. For comparison, the black points represent the asymptotic eigenfunction, cf. (A7). The growth rate of the mode is  $\sigma/(b\Omega) = 1.03 \times 10^{-4}$ .

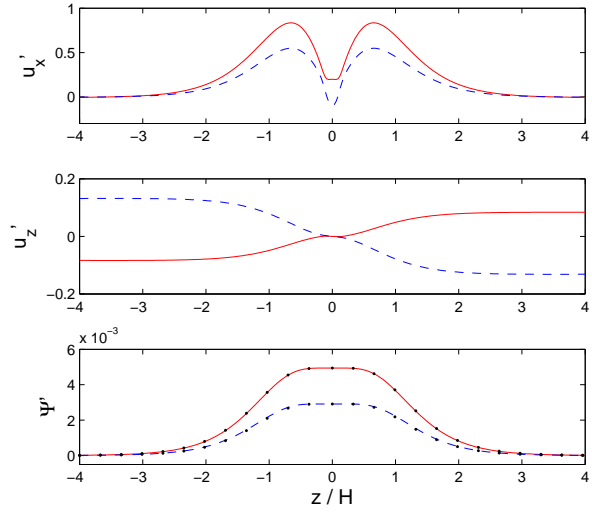


**Figure 9.** The  $u'_x$ ,  $u'_z$  and  $\Psi'$  eigenfunctions of a pinch mode upon the  $n = 2$  channel. Here  $k = 0.05K (= 0.12247)$ ,  $\theta_k = \theta$ , and  $\beta = 1000$ . The growth rate is  $\sigma/(b\Omega) = 2.49 \times 10^{-5} + i5.575 \times 10^{-4}$ , the imaginary part of which is in reasonable agreement with the leading order asymptotic theory, which gives  $\sigma = i5.75 \times 10^{-4}$ . The black points represent the leading order  $\Psi'$  asymptotic profile.

of  $k$ , up to roughly  $K$  itself (where, for  $n = 2$ ,  $K = 2.0796$ ). For small  $k$ , the kink mode growth rate  $\sigma$  scales as  $k$ , while the pinch appears to go as  $\sigma \sim k^3$ . We also plot in Fig. 7 the asymptotic prediction (29) with a dashed line. At low  $k$  it offers excellent agreement with the computed numerical values.

Typical profiles of the two modes are presented in Figs 8 and 9 at small  $k$ , alongside the asymptotic pressure profiles. These low  $k$  modes should rarely be observed because they grow too slowly, but they allow a clearer demonstration of the main physics and a clean comparison with the asymptotic theory. The kink mode in the first figure is easy to distinguish because it possesses a vertical velocity maximum at the centre of the jet,  $z = 0$ . Correspondingly, the pressure perturbation at this point exhibits a strong vertical gradient. As a consequence, the mode elicits an alternating horizontal sequence of upward and downward motions along  $k$ , which will buckle the jet in the familiar Kelvin-Helmholtz pattern. In contrast, the pinch mode in Fig. 9 exhibits a pressure maximum at the jet centre, while  $u'_z$  changes sign. This corresponds to a horizontal sequence of squeezes and rarefactions as fluid is either drawn towards or repelled by the jet.

Other  $\theta_k$  were tried, but only a very narrow range of orientations (around  $\theta$ ) permitted growing modes. As predicted by the criterion (30), the kink mode stabilises when  $|\theta_k - \theta|$  exceeds about 12 degrees. The interval is particularly small because the  $n = 2$  channel is very sub-Alfvénic for  $\beta = 1000$ . Faster growing (larger  $n$ ) channels yield greater  $M_A$  and, consequently, a greater range of unstable  $\theta_k$ . In common with its kink-pinch counterparts in an unstratified disk, the pinch mode grows for a broader range of  $\theta_k$  (GX94, LLB09, Pessah and Goodman 2009, Pessah 2009).

Finally, note that these instabilities will fail to appear

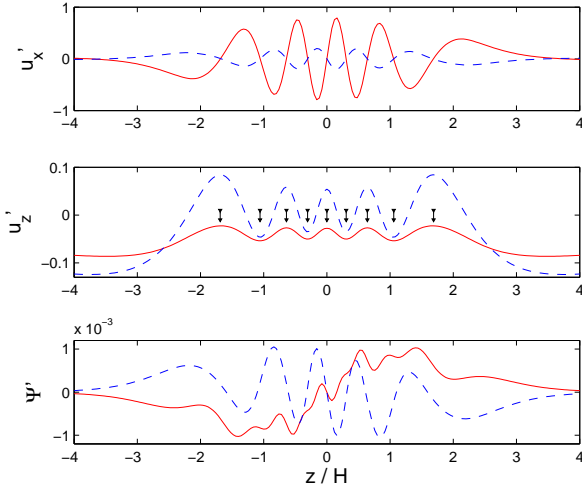


**Figure 10.** Selected components of the kink mode eigenfunction, for parameters:  $n = 10$ ,  $\beta = 1000$ , and  $k = 0.05K (= 0.524)$ ,  $\theta_k = \theta$ . The growth rate of the mode is  $\sigma/(b\Omega) = 3.01 \times 10^{-3}$ . The short vertical arrows in the central panel indicate the locations of the  $n = 10$  MRI channels.

in numerical simulations with short radial domains, such as one scale height  $H$ . Because  $K_2 \approx 2.45/H$ , the radial box length should be at least  $2\pi/K_2 \approx 2.57H$  to capture the shortest horizontal modes. As  $n$  increases for given  $\beta$  this constraint becomes less of a problem: for  $n = 10$  a radial length of  $H$  will comfortably fit a number of growing kink modes.

#### 4.4.2 The $n = 10$ MRI channel flow: 9 jets

Larger  $n$  channels support a greater number of unstable parasitic modes; this is simply because larger  $n$  channels' exhibit more complicated vertical structures and thus permit a wider array of destabilising configurations. The presentation of these many modes at various  $n$  is too lengthy and laborious a task for this paper. Instead we show results from a representative higher order channel, associated with  $n = 10$ .

From Fig. 1, the  $n = 10$  channel flow consists of a jet situated at the midplane  $z = 0$  and a symmetric set of 4 jets on each side. We find that these can harbour up to 9 parasitic modes. These include the kink mode, which grows the fastest and kinks every jet, and 8 kink-pinch modes, which differ in the number and location of their component kinks and pinches. Not every combination of kinks and pinches are supported by the system (if this was so there could be  $\sim 2^9$  such modes!). One important constraint is that no two pinches can attack adjacent jets, a limitation also evident in the unstratified problem (which admits no 'pinch-pinch' modes, LLB09). Some modes also leave a number of jets unmolested, with  $u'_z$  both a maximum and zero at these locations. When  $k$  takes larger values this becomes more noticeable, and the fastest growing modes attack those jets nearest the midplane preferentially.

We plot the eigenfunction of the 'pure' kink mode in Fig. 10 for small  $k$ . Again, we choose small  $k$  modes as they demonstrate the physics the clearest. We deal with

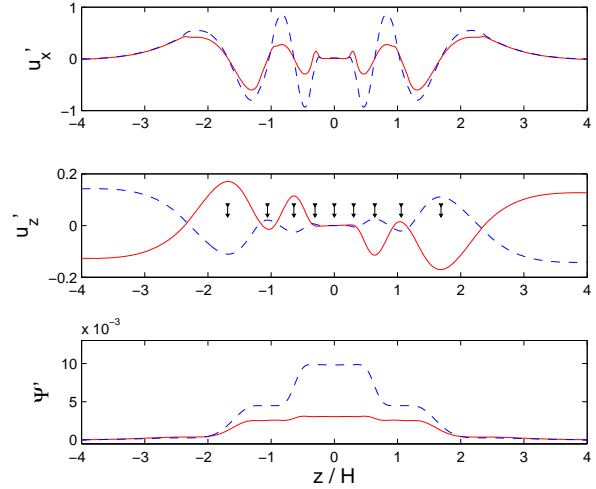


**Figure 11.** Selected eigenfunction components of a kink-pinch mode, with parameters as in Fig. 10. The growth rate is  $\sigma/(b\Omega) = 5.84 \times 10^{-4} - i 3.18 \times 10^{-3}$ . As earlier, the black vertical arrows indicate the locations of the MRI channels. Here the central three channels are pinched as a whole and the remaining channels are kinked.

the fastest growing modes in the following subsection. In the central panel we also indicate the centres of the nine channels by short vertical arrows. These show that the local extrema of the parasite's vertical velocity are located exactly at the channel centres. Thus the mode kinks or buckles every jet concurrently. Simultaneously, the channel centres correspond to those locations where the pressure perturbation possesses a large gradient, though this is less easy to see. Far clearer, is the large-scale antisymmetry in the pressure perturbation, especially in its real part. This means that in addition to the localised kinks upon each channel there exists a 'global' kink upon the *entire* set of jets as well. Variations in the eigenfunctions' large-scale 'envelope' are a feature of the more complicated high  $n$  parasites. In the unstratified analysis, the larger scale structure manifests simply through the Floquet factor  $e^{ik_z z}$  (see GX94 and LLB09). The maximum growth rate for the kink mode (when  $n = 10$ ) is  $\sigma = 0.01726$  achieved when  $k = 0.56K$ . The mode stabilises when  $k \geq 0.97K$ . (Note that for  $n = 10$ , we have  $K = 9.2239$ .)

We present one example of a kink-pinch eigenfunction in Fig. 11. As earlier, the small vertical arrows indicate the locations of the channel centres. The vertical velocity possesses local extrema at all the centres except the jet at the midplane. At the midplane the vertical velocity changes sign, which means this mode pinches the central jet. The other 8 jets, in contrast, are kinked (to varying degrees). The pressure perturbation tells us, on the other hand, that the mode exhibits a large-scale scale envelope through which the entire set of jets is pinched. This is also clear from the large-scale antisymmetry in the  $u'_z$  profile.

#### 4.4.3 Fastest growing modes

The maximum growth rates of the kink mode computed with our stratified model are significantly less than growth rates in the unstratified model (GX94). The unstratified parasitic kink mode reaches a maximum  $\sigma \approx 0.2 b\Omega$  when attacking the fastest growing MRI channel. In contrast,

- when  $\beta = 10^2$ , the  $n = 7$  MRI channel is dominant and its fastest growing parasite possesses  $\sigma = 0.0596 b\Omega$ , at  $k \approx 0.525 K_7$ .
- When  $\beta = 10^3$ , the  $n = 21$  channel is dominant and the maximum  $\sigma$  is  $0.0329 b\Omega$ , at  $k \approx 0.575 K_{21}$ .
- And when  $\beta = 10^4$ , the  $n = 68$  channel dominates and  $\sigma_{\max} = 0.0192 b\Omega$  at  $k \approx 0.585 K_{68}$ .

This discrepancy is something of a surprise. One may have expected that at sufficiently large  $\beta$  the unstratified and stratified results would converge. Instead there appears a scaling, with possibly the logarithm of  $\beta$ , which diverges from the unstratified growth rate. The difference in  $\sigma_{\max}$  probably results from the constraining global structure of the channel flows. While an unstratified parasite attacks an infinite lattice of channels of equal amplitude, its stratified cousins can only attack a *finite* number of channels, of varying amplitude. Consequently, the amount and configuration of the free energy available are dissimilar, and obviously influence the maximum growth rates that parasites can achieve.

Because the fastest growing modes have large  $k$ , the eigenfunctions tend to localise near the midplane where the velocity shear is greatest. They also lose any large-scale envelope they may have exhibited. This can be observed in Fig. 12 which presents the fastest growing mode on the  $n = 21$  channel when  $\beta = 1000$ . Here the mode is individually kinking the middle 12 jets, and ignoring the other 8 at larger altitudes. Because these central jets are more closely packed they offer greater velocity shear for the parasitic mode. This behaviour is typical for the fastest growing modes. It follows that, if they can be adequately resolved, parasites will be found primarily near the midplane in numerical simulations.

A final point concerns the consistency of the intermediate limit we employ. The  $\sigma_{\max}$  of the stratified parasites are not only smaller than their unstratified counterparts, they are sufficiently small to endanger the original scaling  $\sigma \sim b\Omega$ . This means one should revise the lower limit in Eq. (23), which defines the intermediate regime, possibly increasing it to 10 or even 100. But unless  $\beta$  is very large indeed ( $> 10^5$ , say), there may be no intermediate regime to speak of: one must either account for the background shear and channel growth, or one must include compressibility. Having said that, the general features of the analysis — the estimates of the growth rates and the modes' general structure — should offer a satisfactory guide to the parasitic physics at any  $b$ . In the next subsection we discuss the more realistic non-intermediate regimes.

## 4.5 Discussion

Our treatment of the stratified parasitic modes provides only a limited survey of this problem's rich assortment of mode behaviour. But the salient dynamical points remain

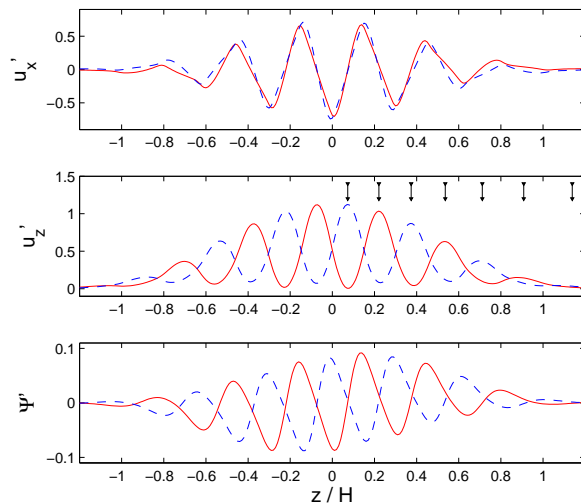


**Figure 12.** Selected eigenfunction components of the kink mode upon the  $n = 21$  channel for  $\beta = 1000$ . The horizontal wavenumber is  $k = 0.575 K (= 12.36)$  and  $\theta_k = \theta$ , thus the growth rate is  $\sigma/(b\Omega) = 0.0329$ . The black vertical arrows indicate the locations of the MRI channels in the range  $1.2 > z > 0$ , a symmetric set occurs for  $z < 0$  but is omitted (there are 20 altogether). Note that the mode has localised upon those channels near the midplane, while ignoring those at larger altitudes. This is typical of larger  $k$  modes, and hence the fastest growing parasites.

clear: the fastest growing mode is always the hydrodynamical kink mode (with  $\theta_k = \theta$ ), favouring a wavenumber some half that of its host channel  $K$ . This is also the case in the unstratified analysis. While there exist an interesting array of other modes, exhibiting complicated morphologies, these pinch and kink-pinch modes grow significantly slower, and so should be dynamically subdominant. In short, if a channel is to be disrupted by a parasite, it will be the kink mode doing the disrupting. Finally, the maximum growth rates that stratified parasitic modes attain are significantly less than those calculated from unstratified models.

#### 4.5.1 Small amplitude channels

Our mathematical characterisation of the parasitic modes only holds in an intermediate limit of channel amplitude: channels must be sufficiently large that we may omit the Keplerian shear and the channels' exponential growth, but sufficiently small that compressible effects are negligible. However, in order to understand the role of the parasites in the MRI dynamics more generally, we need to extrapolate these intermediate results into the regimes of small and large channel amplitudes.

An important dynamical question is: How large will an MRI channel become before it is destroyed by a parasite? Will a channel reach equipartition before collapsing? This is important not only to understand (and possibly control) the MRI's initial eruptive behaviour, but also to assess whether continuous channel production and destruction are key ingredients in MRI-induced turbulence (see Pessah and Goodman 2009, Pessah 2009). In order to answer this question we

must understand the parasites' behaviour when the channel amplitudes are small.

One could, of course, assume that the intermediate amplitude profiles and growth rates (previously calculated) offer a reasonable approximation in the small amplitude regime, as do Pessah and Goodman (2009) and Pessah (2009). This means one expects the exponential growth of the channel and the Keplerian shear to not qualitatively alter the solutions. By simply equating the channel growth rate and the kink mode growth rate, we can obtain a lower bound on the minimum  $b$  necessary for channel disruption. In an unstratified ideal MHD channel this value is roughly 4 (Pessah and Goodman 2009); in the stratified model employed in the previous section with  $\beta = 1000$ , a similar calculation gives  $b_{\min} \approx 15$ . We now argue that both lower bounds are far too small.

In LLB09 the influence of the Keplerian shear and channel growth is discussed in a qualitative way. In that paper the channel growth was emphasised as key in delaying the onset of the parasitic modes. The role of the shear in doing the same was not considered. In fact, the shear should impede the parasites equally efficiently. The Keplerian shear introduces a time-dependence to the parasitic wavevector  $\mathbf{k}$ . As time progresses the orientation angle  $\theta_k$  will decrease and the wavenumber  $k$  will increase. But parasitic modes only grow when their  $\theta_k$  lie within some range encompassing  $\theta$  and when  $k < K$  (see Eq. (30) and Fig. 7, for example). It follows directly that these modes will grow only transiently, enjoying a short burst as  $\theta_k(t)$  and  $k(t)$  pass through their respective neighbourhoods of permitted growth. If the mode does not grow sufficiently fast within this finite time interval — sufficiently fast to reach an amplitude comparable to  $b$  — then the channel remains undisrupted. This time restriction provides a means to calculate the minimum  $b$  necessary for channel disruption. We present these details in Appendix B. There we find that for the unstratified problem, and for an initial parasitic amplitude 1/10 or 1/100 of the channel, the critical amplitude is  $b_{\min} \approx 24$  or 40. In the stratified problem, these values are of order 100. Both estimates are considerably larger than if the Keplerian shear is omitted. Both also show that channels, particularly stratified channels, are destined to achieve large amplitudes and will likely hit equipartition before the parasites can topple them: a channel that has grown from  $b = 1$  to a hundred times that, will have decreased the midplane  $\beta$  by a factor  $10^4$ .

#### 4.5.2 Compressible channels

Once the system has reached equipartition the analyses of Sections 2 and 4 break down. The profile of the MRI channel will alter, its magnetic pressure sufficiently strong to squeeze mass into its jet centres (see Figs 3 and 5 and Stone and Miller 2000). The channel jets will become thinner and more intense, while simultaneously coinciding with narrow current sheets. If sufficiently thin, the influence of resistivity will become important, giving rise to new parasitic tearing modes (explored in LLB09). Finite resolution will ensure that the magnetic reconnection induced by these modes features prominently in stratified box simulations. Compressibility may introduce parasitic Parker modes, which will exploit the strong bands of magnetic field between jet centres. The character of the original kink modes will change as well,

though perhaps not drastically. As shown in LLB09, when the jets narrow and become more intense, the kink mode tends to grow on shorter horizontal length scales, and can split into multiple modes each localised to a single jet. This new wealth of dynamical behaviour should be observable in resolved 3D stratified simulations, and we intend to present some of this work in a later paper.

## 5 CONCLUSION

In summary, we have shown that channel flows, a subset of the linear axisymmetric MRI modes, are approximate nonlinear solutions in the vertically-stratified shearing box, when in the limit of large midplane  $\beta$ . This generalises the better known unstratified result (GX94), but only holds when the equilibrium consists of a net vertical magnetic flux. We compute stratified channel flows numerically for an isothermal model, and confirm the basic result with 1D simulations. The MRI eigenfunctions and growth rates, conversely, offer a valuable numerical benchmark on the performance of codes operating in the vertically-stratified shearing box. In addition, these simulations provide estimates (for future 3D simulations) of the resolution required to resolve the fastest growing channels when using second order numerical schemes: 25 cells per scaleheight are needed when  $\beta = 100$ , 50 cells when  $\beta = 10^3$ , and more than 200 cells per scale height are mandatory when  $\beta = 10^4$ .

Stratified channel flows, like their unstratified counterparts, are subject to a variety of magnetised shear flow instabilities, or 'parasitic modes'. Some of these we directly compute in an intermediate limit of channel amplitude. As in the unstratified setting, the fastest growing parasite is the 'unmagnetised' kink mode. But it is unlikely to destroy its host before equipartition fields have been reached.

At present we are extending these findings with 3D numerical simulations in stratified boxes, where the parasitic modes' behaviour can be confirmed, not only in the initial stages of a simulation but once it has relaxed into a saturated turbulent state. Because of the inevitability of large magnetic fields, and also finite resolution, these simulations will permit a set of interesting physical effects which we have neglected here but which deserve further study. These include, most importantly, magnetic buoyancy and magnetic reconnection. Also, these simulations will allow us to test the recurrent formation of channels once the MRI has saturated in turbulence (Suzuki and Inutsuka 2009). In particular, they can establish whether larger radial domains impede recurrent channel formation, by analogy with unstratified boxes (Bodo et al. 2008, LLB09).

Lastly, we speculate on the potential role dominant channel flows play in real magnetised accretion disks. Global disk models support analogues of the stratified MRI channels, localised in radius to narrow rings. Such modes might also exhibit a weaker version of the nonlinear property examined in this paper, permitting one mode to dominate the initial evolution of small amplitude initial conditions. Indeed, simulations with a poloidal field piercing the disk report such behaviour (Hawley 2000, 2001). In fully-developed turbulent disks, on the other hand, the dominance of a single channel will be rare. But occasional 'run-away' channel flows might occur in the marginally stable fluid that divides re-

gions of stable and unstable MRI — dead-zone interfaces in protostellar disks, for instance. It may take only a small fluctuation in the ionisation and thermal properties of the gas to ignite instability in this previously quiescent critical layer, and hence launch a powerful MRI channel flow. Disruptive events of this kind may control the integral-scale intermittency that should characterise the dead-zone interface, and may even be related to the initial phases of outburst behaviour (Zhu et al. 2009). Similarly, channel flows may also feature in the onset of episodic accretion in dwarf nova disks (Gammie and Menou 1998).

## ACKNOWLEDGMENTS

The authors acknowledge the careful and detailed report by the anonymous reviewer, which led to a much improved manuscript. HNL and SF would like to thank Alexandros Alexakis, Steven Balbus, Tobias Heinemann, Pierre Lesaffre, Geoffroy Lesur, and Pierre-Yves Longaretti for helpful advice. HNL acknowledges funding from the Conseil Régional de l’Île de France. SF acknowledges the Isaac Newton Institute for Mathematical Sciences for hospitality during August 2009 during which most of the numerical simulations presented in the paper were completed. Such simulations were granted access to the HPC resources of CINES under the allocation x2009042231 made by GENCI (Grand Equipement National de Calcul Intensif). OG would like to thank the CEA Service Astrophysique for its hospitality, and where some of the numerical simulations were undertaken.

## REFERENCES

Arfken, G., 1970. *Mathematical methods for physicists* (2nd ed.). Academic Press, London.

Balbus, S. A., Hawley, J. F., 1991. *ApJ*, 376, 214.

Balbus, S. A., Hawley, J. F., 1992. *ApJ*, 400, 610.

Balbus, S. A., Hawley, J. F., 1998. *Rev. Mod. Phys.*, 70, 1.

Barranco, J. A., Marcus, P. S., 2005. *ApJ*, 623, 1157.

Bickley, W. G., 1937. *Phil. Mag.*, 23, 727.

Biskamp, D., Schwarz, E., Zeiler, A., 1998. *Phys. Plasmas*, 5, 2485.

Blackman, E. G., Pessah, M. E., 2009. *ApJ*, 704, 113.

Bodo, G., Mignone, A., Cattaneo, F., Rossi, P., Ferrari, A., 2008. *A&A*, 487, 1.

Boyd, J. P., 2000. *Chebyshev and Fourier Spectral Methods* (2nd ed.). Dover Publications, New York.

Brandenburg, A., Nordlund, A., Stein, R. F., Torkelsson, U., 1995. *ApJ*, 446, 741.

Davis, S. W., Stone, J. M., Pessah, M. E., 2010. *ApJ*, submitted (arXiv:0909.1570).

Drazin, P. G., Reid, W. H., 1982. *Hydrodynamic stability*. Cambridge University Press, Cambridge UK.

Fleming, T., Stone, J. M., 2003. *ApJ*, 585, 908.

Fromang, S., Hennebelle, P., Teyssier, R., 2006. *A&A*, 457, 371.

Gammie, C. F., Balbus, S. A., 1994. *MNRAS*, 270, 138.

Gammie, C. F., Menou, K., 1998. *ApJL*, 492, L75.

Gilman, P. A., Glatzmaier, G. A., 1981. *ApJS*, 45, 335.

Goldreich, P., Lynden-Bell, D., 1965. *MNRAS*, 130, 125.

Golub, G. H., Van Loan, C. F., 1996. *Matrix Computations* (3rd ed.). John Hopkins Uni Press, Baltimore.

Goodman, J., Xu, G., 1994. *ApJ*, 432, 213.

Gough, D. O., 1969. *JatS*, 26, 448.

Hawley, J. F., 2000. *ApJ*, 528, 462.

Hawley, J. F., 2001. *ApJ*, 554, 534.

Hawley, J. F., Gammie, C. F., Balbus, S. A., 1995. *ApJ*, 440, 742.

Hirose, S., Krolik, J. H., Stone, J. M., 2006. *ApJ*, 640, 901.

Johansen A., Levin, Y., 2008. *A&A*, 490, 501.

Latter, H. N., Lesaffre, P., Balbus, S. A., 2009. *MNRAS*, 394, 715.

Liverts, E., Mond, M., 2009. *MNRAS*, 392, 287.

Meshalkin, L., Sinai, Y., 1961. *J.Appl.Math.Mech.*, 25, 1700.

Miller, K. A., Stone, J. M., 2000. *ApJ*, 534, 398.

Ogilvie, G. I., 1998. *MNRAS*, 297, 291.

Ogilvie, G. I., Livio, M., 2001. *ApJ*, 553, 158.

Papaloizou, J., Szuszkiewicz, E., 1992. *GAFD*, 66, 223.

Pessah, M. E., 2009. eprint arXiv:0908.1791

Pessah, M. E., Goodman, J., 2009. *ApJ*, 698, 72.

Salmeron, R., Wardle, M., 2003. *MNRAS*, 345, 451.

Salmeron, R., Wardle, M., 2005. *MNRAS*, 361, 45.

Salmeron, R., Wardle, M., 2008. *MNRAS*, 388, 1223.

Salmeron, R., Königl, A., Wardle, M., 2007. *MNRAS*, 375, 177.

Sano, T., 2007. *Ap&SS*, 307, 191.

Sano, T., Miyama, S. M., 1999. *ApJ*, 515, 776.

Sano, T., Inutsuka, S., 2001. *ApJ*, 561, 179.

Shi, J., Krolik, J. H., Hirose, S., 2010. *ApJ*, 708, 1716.

Stone, J. M., Hawley J. F., Gammie C. F., Balbus S. A., 1996. *ApJ*, 463, 656.

Suzuki, T. K., Inutsuka, S., 2009. *ApJ*, 691, 49.

Teyssier, R., 2002. *A&A*, 385, 337.

Zhu, Z., Hartmann, L., Gammie, C., McKinney, J. C., 2009. *ApJ*, 701, 620.

Ziegler, U., 2004. *JCoPh*, 196, 393.

## APPENDIX A: ASYMPTOTIC ANALYSIS OF PARASITIC INSTABILITIES

In this appendix we sketch out an asymptotic solution to Eqs (25)–(27) in the limit of small horizontal parasitic wavenumber:  $0 < k \ll 1$ . We concentrate on a description of the kink mode as it is the fastest growing, and hence most dynamically significant.

First we manipulate the governing equations into single second order equation for the pressure perturbation  $\Psi$ :

$$g(z) \frac{d}{dz} \left( \frac{1}{g(z)} \frac{d\Psi}{dz} \right) - k^2 \Psi = 0, \quad (\text{A1})$$

where

$$g(z) = h(z) [\sigma + ikMF_n(z) \cos \Delta]^2 + \frac{2}{\beta} k^2 G_n(z)^2 \sin^2 \Delta. \quad (\text{A2})$$

recall  $\Delta = \theta - \theta_k$ , which is just the difference in orientation angles of the MRI channel and its parasite, and  $M$  is the Mach number. The algebra required to derive this can be greatly reduced by using Lagrangian displacements, not momenta (see GX94). The reader will notice that Eq (A1) is similar to Eq. (25) in GX94. We can reproduce this equation if we solve instead for the Lagrangian vertical displacement and assume the disk is unstratified. One can derive an analogous ‘semicircle theorem’ for (A1) which shows that both the growth rate and frequency of the parasite is bounded above by  $k$ . Thus as  $k$  goes to 0, so must both the real and imaginary part of  $\sigma$ .

### A1 Kink modes

We now suppose that  $k$  is sufficiently small that we may drop the last term in Eq. (A1). This assumption stipulates that the horizontal variation of the parasite is much greater than

its vertical variation, as well as variations in the channel and the equilibrium density (which are of order  $H$  at most).

We can solve directly, in this case, for  $\Psi$ :

$$\Psi = c_1 + c_2 \int_{-z_B}^z g(\hat{z}) d\hat{z}$$

where  $c_1$  and  $c_2$  are integration constants and  $z_B$  is the upper boundary of the disk (and may be  $\infty$ ). We require that  $\Psi = 0$  at  $z = \pm z_B$  (the vanishing boundary conditions). This furnishes  $c_1 = 0$  and the eigenvalue equation

$$\int_{-z_B}^{z_B} g dz = 0.$$

After some manipulation we obtain the growth rate explicitly:

$$\sigma^2 = A_n k^2 M^2 [\cos^2 \Delta - M_A^{-2} \sin^2 \Delta], \quad (\text{A3})$$

where

$$A_n = \left( \int_{-z_B}^{z_B} h F_n^2 dz \right) / \left( \int_{-z_B}^{z_B} h dz \right). \quad (\text{A4})$$

The Alfvénic Mach number  $M_A = u_0/v_A^0$  has been introduced in the above, which can be re-expressed in terms of  $M$  and  $\beta$ . In deriving equation (A3) the following two identities were required

$$\int_{-z_B}^{z_B} h F^2 dz = \int_{-z_B}^{z_B} G^2 dz, \quad \int_{-z_B}^{z_B} h F dz = 0,$$

the first follows from multiplying Eq. (17) by  $F$  and integrating, the second from the relationship between  $F$  and  $dG/dz$ .

As anticipated, the growth rate scales like  $k$  and will be real (and positive) unless

$$|\theta - \theta_k| > \arctan M_A, \quad (\text{A5})$$

which is precisely the stability condition we find in the unstratified case for kink modes (see GX94, and LLB09). The criterion just says that if a parasite is to grow, its wavevector must point sufficiently along the shear flow.

The eigenfunctions can be obtained analytically if we use the ‘approximate isothermal model’ (cf. Section 2.4.3). Then  $A_n = 1/(2n + 1)$ , and in the hydrodynamical case of  $\theta_k = \theta$  we obtain

$$\Psi_{1k} \propto \text{sech}^2 z \left( \tanh z - i\sqrt{3} \right), \quad (\text{A6})$$

$$\Psi_{2k} \propto \tanh z \text{sech}^4 z \left[ (5 - 4 \cosh 2z) + 2i\sqrt{5}(1 + \cosh 2z) \right] \quad (\text{A7})$$

for  $n = 1$  and  $n = 2$  respectively. The  $\Psi_{2k}$  eigenfunction is plotted in Fig. 8, and provides a check on the full numerical solution.

Finally note that if the disk is unstratified we can compute  $A_n = 1/2$  if the limit of  $z_B \rightarrow \infty$  is taken carefully in both the denominator and numerator of (A4) (see also GX). Interestingly, this prefactor is independent of the mode number or  $K$ , in contrast to the stratified case of the previous paragraph where larger  $n$  furnishes slower growing modes at small  $k$ . According to Section 4.5.1 this seems also to be the case for general  $k$ .

## A2 Pinch and kink-pinch modes

The mathematical derivation of the pinch and kink-pinch modes is a great deal more involved and subtle, not least because the real part of the growth rate  $\sigma$  comes in at higher orders. We will not produce the full analysis here. Instead, we work out the problem for the simple  $n = 2$  case to leading order.

The  $n = 2$  MRI mode is a single jet centred at  $z = 0$ . It follows that there are two types of parasite: odd (kink modes) for which  $\Psi(0) = 0$ , and even (pinch modes) for which  $d\Psi/dz(0) = 0$ . At leading order the latter boundary condition gives the equation:

$$g(0) = 0,$$

which is satisfied only if

$$\sigma = -ikM F(0) \cos \Delta. \quad (\text{A8})$$

Applying the decaying boundary condition at  $z = z_B$  completes the description of the pinch mode, the vertical profile of which is

$$\Psi \propto 1 - \left( \int_0^z g(\hat{z}) d\hat{z} \right) / \left( \int_0^{z_B} g dz \right), \quad (\text{A9})$$

on the domain  $z \in [0, z_B]$ . If we apply the approximate isothermal model and furthermore take  $\theta = \theta_k$ , then this reduces to

$$\Psi_{2p} \propto 1 - \tanh^5 z. \quad (\text{A10})$$

The eigenfunction is plotted in Fig. 9 against the numerical solution. The real part of the growth rate comes in at higher order and requires an additional asymptotic matching procedure, the details of which we do not provide here.

## APPENDIX B: SMALL AMPLITUDE CHANNELS

The purpose of this appendix is to derive an estimate for the smallest amplitude  $b$  that permits parasitic modes to overcome the primary channel flow. Channels with amplitudes below this critical value host parasites that grow too slowly to cause disruption. We define ‘channel disruption’ when the *amplitudes* of the channel and the parasite are equal, in contrast to when their *growth rates* are equal (Pessah and Goodman 2009, Pessah 2009). In the following, the influence of the background shear will be included, and we will find that it is a primary agent delaying channel disruption. We do not treat the influence of the Coriolis force.

For simplicity, the disk is assumed to be *unstratified*. Consider the fastest growing MRI channel, with  $s = (3/4)\Omega$  and  $\theta = \pi/4$ . Its fastest growing parasite, the one in which we will be most interested, is the kink mode. It achieves its maximum growth when  $\theta_k = \theta = \pi/4$  and  $k \approx 0.6K$ , at which point  $\sigma \approx 0.2b\Omega$ . It, however, can grow at a reduced rate within the sector  $|\theta - \theta_k| < \theta_{\text{crit}} < \pi/4$ , and for  $k < K$  (see GX94).

Suppose that we allow for the background shear’s effect on the parasitic wavevector  $\mathbf{k}$ . Under its influence the wavevector will become time-dependent, lengthening with time and rotating so that it points more and more radially. These changes are summarised by

$$k_x(t) = k_x^0 + \frac{3}{2}\Omega k_y^0 t, \quad (\text{B1})$$

where  $(k_x^0, k_y^0)$  is the initial value of the wavevector. Note that the azimuthal component  $k_y^0$  is independent of time.

We analyse a fiducial kink mode with  $k_y^0 = (0.6/\sqrt{2})K$  and  $k_x^0 = 0$ .<sup>1</sup> Thus the kink mode starts out with a purely azimuthal wavevector and zero growth rate. It, however, will achieve the maximum growth possible at some later time when  $k_x = k_y$ , i.e. when  $\mathbf{k}$  is perfectly aligned with the channel. After passing this ‘sweet spot’ its growth rate will decline, and when  $k_x^f = \sqrt{0.82}K$  it will be zero, because at that point  $k = K$ . If we permit the mode to grow between orientations  $k_x = 0$  and  $k_x = k_x^f$ , we can then estimate the total time the mode grows from Eq. (B1). We have, in fact,

$$t = \frac{2(k_x^f - k_x^0)}{3\Omega k_y^0} \approx 1.42 \Omega^{-1}. \quad (\text{B2})$$

The growth time allotted to a kink mode is thus roughly a quarter of an orbit. This is the maximum time available for it to disrupt its host. If it cannot reach a sufficiently large amplitude within this time then the channel will keep growing unimpeded (until another kink mode emerges and tries its luck). Of course, the success of the parasite’s attack depends on the average size of  $\sigma$  over the period of growth. We can, in fact, easily derive a minimum value for this average growth rate, below which a kink mode cannot disrupt the channel. And because  $\sigma$  is proportional to  $b$ , this in turn allows us to calculate the minimum  $b$  below which channels are safe from kink modes.

To ease the calculation we shall take this average value to be half the maximum growth, i.e.  $\sigma_{\text{av}} = 0.1 b\Omega$ . We also must attribute a starting amplitude to the channel, which we take to be  $Rb$ , where  $R$  is some fraction. During the time  $t = 1.42/\Omega$ , the channel will grow by approximately  $e^{1.07}$ , while the kink mode will grow by approximately  $e^{0.142b}$ . The ratio of their amplitudes at the end of this time is hence

$$\frac{\text{parasite amplitude}}{\text{channel amplitude}} \approx R \exp(0.142 b - 1.07). \quad (\text{B3})$$

If this ratio is set to 1, then we can calculate the critical (minimum)  $b$ . We have simply

$$b_{\text{cr}} \approx 7.54 - 7.04 \ln R. \quad (\text{B4})$$

If the initial parasitic amplitude is set to one tenth the channel, i.e.  $R = 1/10$  then the minimum  $b$  for channel disruption is about 24, while  $R = 1/100$  gives  $b_{\text{cr}}$  closer to 40. In either case, channels will grow to significantly larger amplitudes than predicted by Pessah and Goodman (2009) and Pessah (2009), who neglect the influence of the background shear in retarding the parasitic growth.

The analysis above was carried out for the unstratified problem, but it is easy to generalise to the stratified disk. As mentioned in Section 4, the stratified parasitic growth rates are smaller than unstratified ones. If this is taken into account we obtain  $b_{\text{cr}} \sim 100$  for both  $R = 1/10$  and  $R = 1/100$ . Consequently, by the time a parasite can make a successful attack, the channel will have reached enormous amplitudes, decreasing the midplane plasma beta by a factor

$10^4$ . By then it is more than likely that equipartition has been reached.

<sup>1</sup> We assume that a kink mode poses the greatest threat to channel stability. Though pinch and kink-pinch modes grow for a larger range of  $\theta_k$ , they grow for a smaller range of  $k$ . This combined with their smaller growth rates leads us to discount them.